Measurement and analysis of the structural performance of cellular metal sandwich construction

H. Bart-Smith[a,*], J.W. Hutchinson[a], A.G. Evans[b]

[a]*Division of Engineering and Applied Sciences, Harvard University, Pierce Hall, Cambridge, MA 02138, USA*
[b]*Materials Institute, Princeton University, Princeton, NJ 08540, USA*

Abstract

The bending performance of sandwich construction with thin cellular metal cores has been measured and simulated. A mechanism map has been generated to characterize the predominant failure phenomena based upon collapse load criteria for face yielding, core shear and indentation. A previously developed constitutive law for the core material has been incorporated into numerical simulations. Comparisons have been made with the measured response. Initial discrepancies attributed to a core thinness effect were rectified by inputting core shear properties measured on materials having the same thickness. Analytical estimates for the stiffness, yield load and limit load are compared with the numerical simulations and experimental results. © 2001 Elsevier Science Ltd. All rights reserved.

1. Introduction

Cellular metals have strength and stiffness attributes that suggest their application as cores for ultra-light panels [1–3]. The benefits of cellular sandwich construction, relative to competing concepts, arise primarily in curved configurations where the isotropy of the cellular material is advantageous [1,2]. Before envisaging specific implementations, the preference for sandwich construction with a cellular core must be demonstrated by simulation and measurement, as predicated on an ability to simulate their response in various structural forms. For this purpose, a constitutive law representative of the core material bonded to face sheets must be available, fully validated by experimental measurements. While a basic constitutive law for cellular metals has been proposed [4] it remains to establish its application to cores bonded to face sheets in typical

---

* Corresponding author.
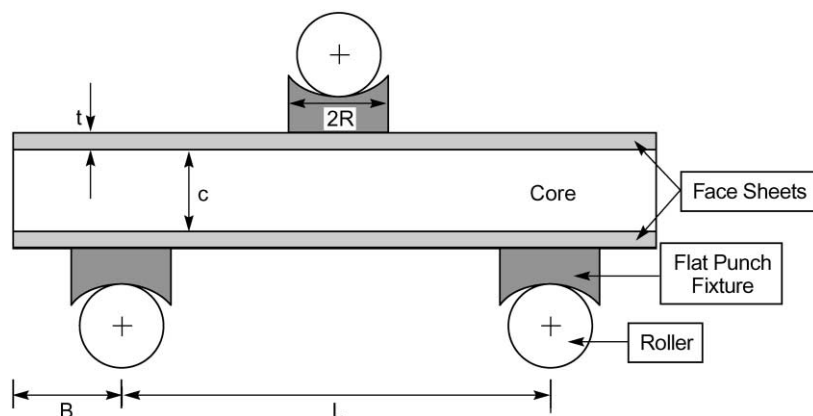*E-mail address:* hbs@princeton.edu (H. Bart-Smith).

Fig. 1. The three-point flexure configuration used to experimentally probe the core-dominated failure mechanisms.

sandwich construction. The present study addresses this deficiency by evaluating the performance of thin sandwich panels comprising a commercial closed-cell Al alloy (trade name Alporas; [5,6]) bonded to Al face sheets. Such construction has particular interest as lightweight panels and shells in the aerospace and automotive sectors [1].

The approach is as follows. A simple test configuration capable of probing each of the deformation and failure modes expected for panels with thin cores is selected. Bending configurations are found to be appropriate for this purpose (Fig. 1). Based upon collapse load considerations, mechanism maps are constructed [1]. The maps identify domains wherein failures occur preferentially by a single mechanism: either by core indentation, face sheet yielding or core shear (see captions to Figs. 4 and 5).[1] The coordinates comprise the ratios of the face sheet thickness, t, and the core thickness, c, to the load span, L. From the maps, bending configurations are designed to measure the actual modes of deformation and failure. Comparison between the measurements and simulations identify deficiencies in the constitutive description. Changes in the latter are made based on insights gained from observations of failure mechanisms, until a consistent representation has been found. An available constitutive law for cellular metals [5] has been used to perform the simulations.

2. Materials

Sandwich panels were manufactured by using an Alporas core [5,6], with two Al alloy face sheet materials (Table 1). One face material (designated 6061-0) was relatively soft and amenable to yielding in the flexure tests. The other (designated 6061-T6) had a sufficiently high yield strength such that core-related failures dominate. To produce these panels, thin sheets (5 and 10 mm) of

---

[1] Other failure modes found in honeycombs, such as face sheet wrinkling and debonding [7], are not normally encountered in optimized cellular metal panels.

Table 1
Material properties

(i) *Face sheet materials*		
Aluminum alloy	Young's modulus E_f (GPa)	Yield strength σ_Y (MPa)
6061-0	69	80
6061-T6	69	268

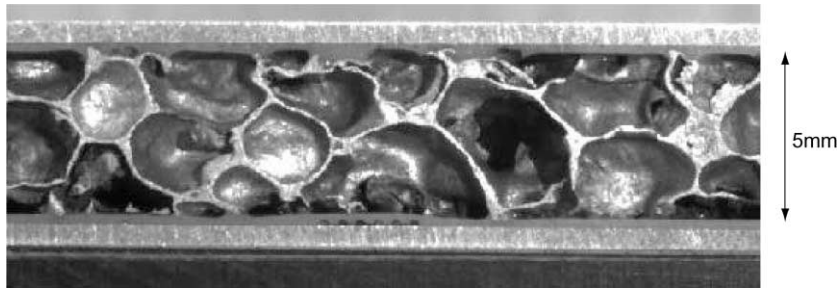| (ii) *ALPORAS core material*	
Relative density	0.08
Young's modulus, E_c (GPa)	0.23
Shear modulus, G_c (GPa)	0.09
Uniaxial yield strength, σ_Y (MPa)	1.5
Plastic Poisson ratio, v^P	0
Elastic Poisson ratio, v	0.3
Yield coefficient, β	$3\sqrt{2}$

Fig. 2. Optical image of cross section of a sandwich beam.

Alporas were cut from castings using electro-discharge machining. Bonding was achieved by using thin layers of the adhesive FM-300 (manufactured by Cytec), frequently used in the aerospace industry. Prior to bonding, the face sheets and core were degreased by streaming condensed trichloroethylene over the surfaces. Thereafter, the face sheets were primed to improve the bond, as well as to protect the surface from subsequent oxidation. For bonding purposes, the adhesive was placed between the primed face sheets and Al core. Curing was conducted in an autoclave for 2 h at 175°C, subject to a normal pressure of $\sim$ 2.8 kPa. The final structure had a residual polymer layer $\sim$ 100 μm thick, embedding the core (Fig. 2).

   The face sheet materials were tested in tension, following ASTM Standard E8, to determine their yield strength, Young's modulus and strain hardening coefficient. These tests were required for mechanism map construction and for numerical simulations, because of possible effects of the bonding process on the mechanical properties. It was found that, because of the temperatures involved, bonding elevated the yield strength of the softer aluminum alloy (6061-0): whereas there was no discernable effect on the strength of the stronger 6061-T6 alloy. The Young's modulus was unchanged in both cases.

3. Mechanism maps

To simulate the core, a constitutive law developed by Deshpande and Fleck [4] was used. According to this law, the yield strength of the cellular material can be expressed using the potential.

$$\Phi \equiv \hat{\sigma} - \sigma_c \leqslant 0, \tag{1}$$

where Φ represents the yield surface, σ_c is the yield strength of the core in uniaxial compression and $\hat{\sigma}$ is an effective equivalent stress, defined as

$$\hat{\sigma}^2 = \frac{[\sigma_e^2 + \alpha^2 \sigma_m^2]}{[1 + (\alpha/3)^2]} \tag{2a}$$

with σ_e the von Mises stress and σ_m the mean stress. The hydrostatic strength of the material is

$$|\sigma_m| = \left[\frac{1 + (\alpha/3)^2}{\alpha^2} \right]^{1/2} \sigma_c. \tag{2b}$$

The parameter α characterizes the aspect ratio of the elliptical yield surface when expressed in (σ_e, σ_m) space. This model appears to be consistent with experimental measurements, given an appropriate choice of α [4]. The equivalent plastic strain increment (for associated flow) is expressed in terms of the equivalent stress by

$$\dot{\varepsilon}_{ij}^p = \frac{\dot{\hat{\sigma}}}{H} \left[\frac{\partial \Phi}{\partial \sigma_{ij}} \right], \tag{3}$$

where H is the hardening modulus. The assumption that the plastic strain rate $\dot{\varepsilon}_{ij}^p$ is normal to the yield surface (associated flow) allows the plastic Poisson ratio v^p to be specified as a function of α.

$$v^P \equiv -\frac{\dot{\varepsilon}_{11}^p}{\dot{\varepsilon}_{33}^p} = \frac{1/2 - (\alpha/3)^2}{1 + (\alpha/3)^2}. \tag{4}$$

The dependence of α on v^p is shown in Fig. 3 [1]. The Alporas material has a plastic Poisson ratio of approximately zero [8] such that $\alpha \approx 2.12$.

Based on analytical considerations and this constitutive representation, it has been possible to derive expressions that describe the critical loads needed to either initiate yielding or cause collapse. A brief description of each failure load expression is given in the appendix. In turn, these can be used to construct failure-mode maps. Such maps are generated here (Figs. 4 and 5) for a sandwich beam subject to three-point flexure, with the flat-punch loading depicted in Fig. 1. These maps identify regions of dominant failure. By changing the design of each beam, the different failure regions can be probed, as well as the accuracy of the boundaries between mechanisms.

The mechanism maps constructed for both of the face sheet materials are presented in Figs. 4 and 5, with c/L and t/L as the coordinates. They have been constructed using the limit load results (see the appendix), because of the substantial load-bearing capacity of the beams beyond initial yield (see Fig. 6). The domains in Fig. 4 were constructed with $R/L = 0.05$. Fig. 5 displays the influence of R/L on the boundaries between failure mechanisms. As expected, upon reducing R/L, the incidence of indentation increases. For configurations made with the high-strength (6061-T6) face sheets, face yielding is not operative in practical ranges of specimen dimensions: only
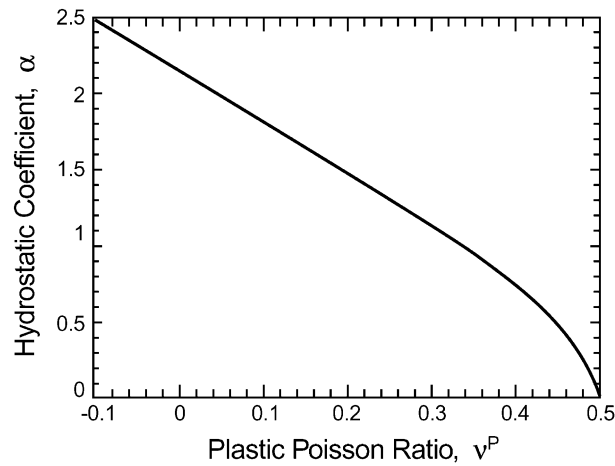
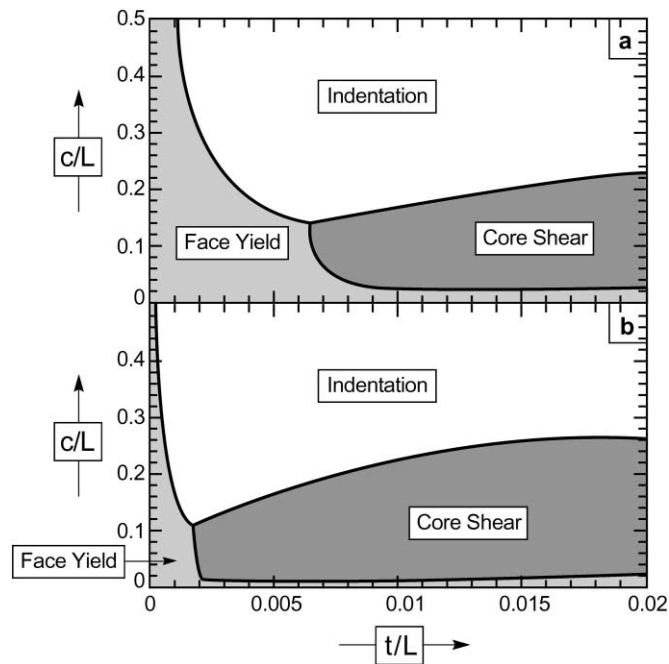Fig. 3. The dependence of the hydrostatic coefficient α on the plastic Poisson ratio, v^p.

Fig. 4. Mechanism maps showing failure domains for two different face sheet materials, $R/L = 0.05$.

indentation and core shear appear on the map. Conversely, face yielding emerges as a potential failure mode when the softer material, 6061-0, is used.

These maps are used to settle upon dimensions of the specimens used to experimentally probe the failure mechanisms. The beam dimensions are designed to probe all three mechanisms. Table 2 gives some examples of beams tested.
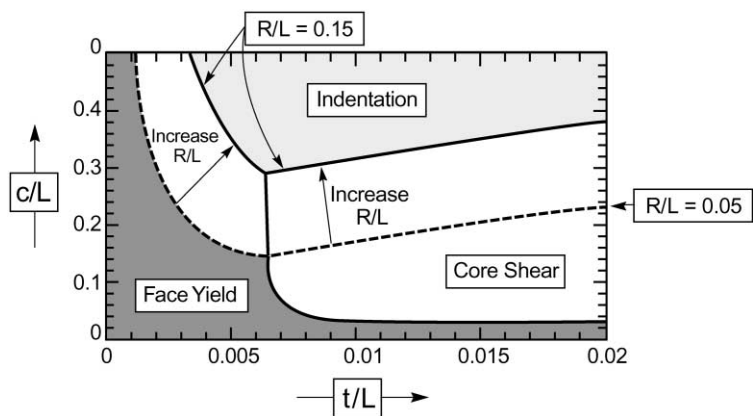
Fig. 5. Mechanism map showing influence of R/L on the boundaries between the failure modes.
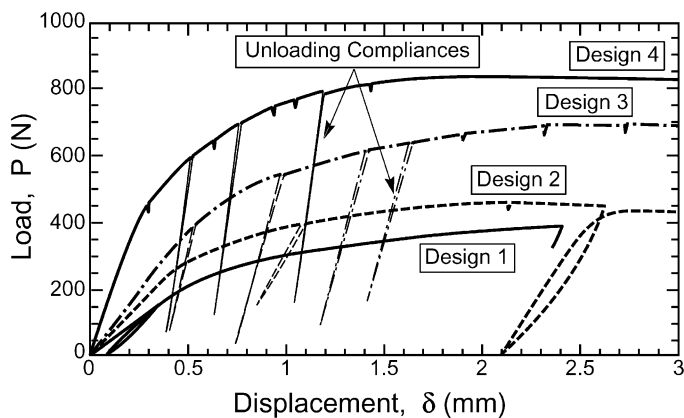

Fig. 6. Measured load–deflection curves.

Table 2
Specimen design — examples

Design #	Face sheet	Failure mode	t/L	c/L	t (mm)	c (mm)	L (mm)	R/L
1	6061-0	FY	0.0025	0.0625	0.4	10	160	0.15
2	6061-T6	CS	0.01	0.0625	0.8	5	80	0.1
3	6061-T6	CS	0.01	0.125	0.8	10	80	0.05
4	6061-T6	I	0.01	0.25	0.8	10	40	0.05

4. Measurements

The flat platten fixtures were manufactured from high-strength steel and attached using an epoxy. Loads were applied using a servo-electric load frame, while measuring the load and center point displacements. Optical images of the side faces were taken throughout the tests using a long focal length optical telescope. These images were used to characterize the predominant deformation mechanisms. A strain gauge was placed on the underside of the specimen directly below the center loading platten.

Measured load/deflection curves are summarized in Fig. 6. Periodic load/reload curves show that the initial bending stiffness is appreciably softer than that associated with unloading. This same characteristic has been found for the core material when tested either in uniaxial compression or shear [6]. All of the curves have similar shapes: wherein the system strain hardens beyond the initial linearity and then approaches a maximum (or asymptotic) load. However, there are appreciable differences in the peak load among configurations, which remain to be related to the operative mechanisms in the following section. For each design there is a variation of about 15% in the peak load between nominally identical specimens.

Optical images of several configurations before and after testing (Fig. 7) reveal the predominant failure modes. In general, beams expected to fail by core shear exhibit shear displacements between the central and outer loading plattens, with minimal indentation (Fig. 7a). Moreover, configurations expected to be indentation-dominated exhibit a marked reduction in face sheet spacing beneath the central platten (Fig. 7b). This correspondence is elaborated for two of the designs expected to exhibit core shear failure (designs 2, 3). For these designs, the upper bound result (Eq. (A.10)) has been used to construct the failure maps. It asserts that plastic hinges form at the outer supports such that all core shearing takes place between the load points and not in the overhang. The experimental images (Fig. 7a) affirm that there are no shear displacements in the overhang.

The broad correspondence of the failure modes revealed by the optical images with those anticipated from the analytical model substantiates the utility of this approach for establishing preliminary failure maps.

5. Bending simulations

5.1. Finite element method

The commercial finite element code, ABAQUS, has been used to simulate the load/deflection response, as needed to compare with the measurements of Figs. 6 and 7. A user-defined subroutine for the material constitutive law has been generated, based upon the preceding description for metallic foams [9]. In defining the core and face sheet materials, 8-noded plane strain elements were used. The adhesive between face and core was not simulated. Displacement boundary conditions were applied at nodes over a distance equivalent to the width of the flat platten, $2R$. The beam was simply supported, but with the imposition of multi-point constraints at nodes about the roller. The latter restricts nodes between designated masters to motion about a single rotating axis
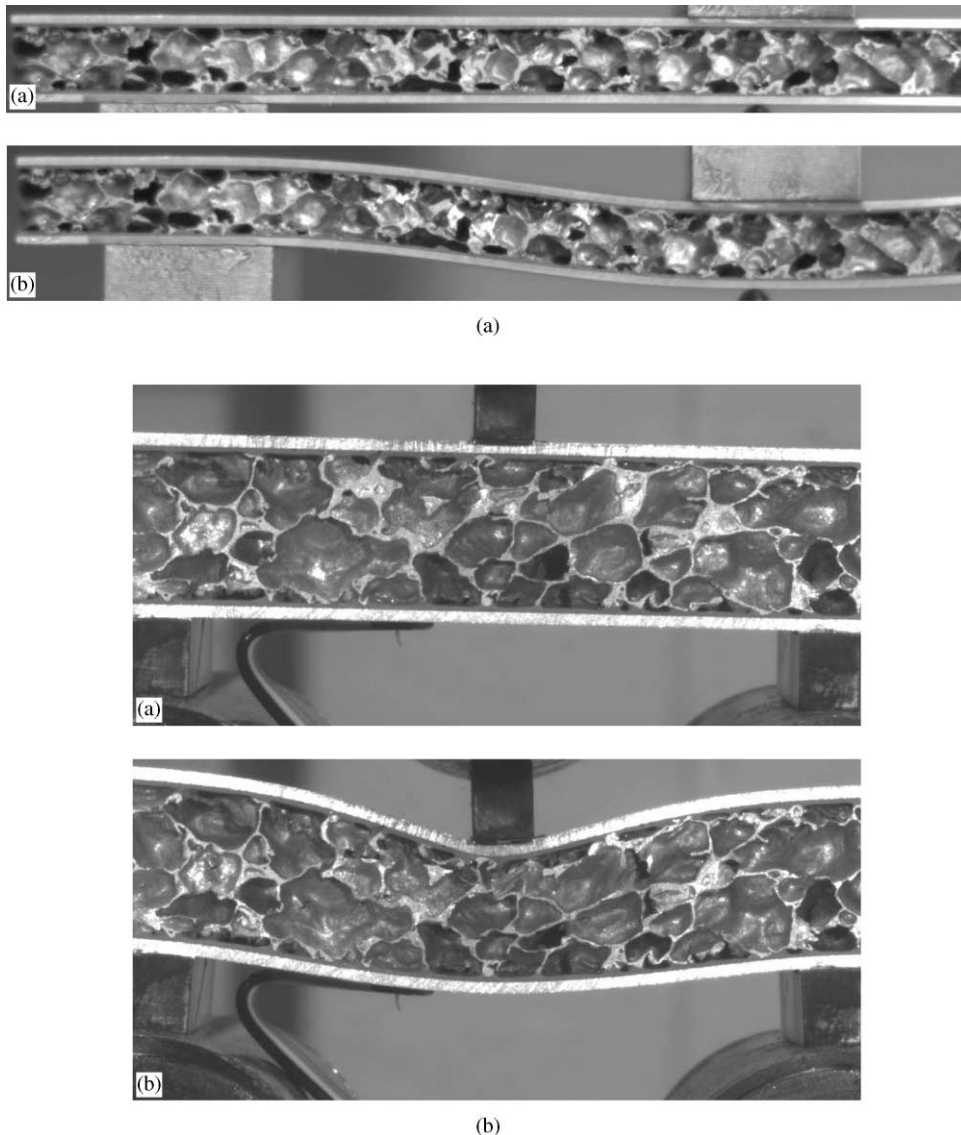
(a)

(b)

Fig. 7. Optical images for specimens expected to fail by (a) core shear and (b) indentation.

(ABAQUS manual). In order to ensure a convergent solution, the number of elements was increased until the results remained invariant.

The uniaxial tensile test measurements performed on the face materials (Table 1) were used as the material description within the input file. (To simplify the simulations, for those designs wherein face yielding was not expected, the face material was treated as elastic-perfectly plastic.) The compressive stress–strain response independently measured on the Alporas material [6] has been used to characterize the yield surface of the core. Such input data would be appropriate for thick

cores. A core thinness effect is expected for the present configurations (thickness 5 and 10 mm). This effect is attributed to constraints on deformation imposed at locations where the cell walls of the core are attached to the face. That is, the cell walls bonded to the face sheet experience more constraint than cell walls in the interior. To model this effect, the core strength levels have been elevated by 30% above those measured for the bulk material, consistent with shear measurements obtained on thin specimens by Andrews et al. [10,14].

For the basic simulations, the "soft" initial loading modulus for the Alporas material ($E_c = 0.23$ GPa) [8] has been used, to be consistent with the sandwich beam test protocol. The unloading modulus (1.15 GPa) has been used to simulate the unloading curves.

5.2. Load/deflection curves

Characteristic load/deflection curves calculated with and without core thinness adjustments are presented in Figs. 8a–d. Note that, in cases where failure is dominated by the core, the maximum loads calculated using the bulk core properties and those for thin cores bound the experimentally measured loads. The former underestimates the loads, while the latter yield a slight overestimate. Nevertheless, the correspondence between the measurements and the simulations is generally as good as can be expected, given the variability in the properties of the core material [10]. The comparisons are elaborated in the following section. Specific load/deflection features are as follows. (i) Following yielding, there is strong strain hardening, despite the non-hardening nature of the core material. (ii) In core-shear configurations, within the range of displacements considered, the load asymptotically approaches a limit (Figs. 8a and b). (iii) Configurations that reside within the core indentation domain exhibit a load maximum (Fig. 8c). (iv) When face yield dominates, the loads reached are dependent on the strain-hardening coefficient for the face material, as illustrated by simulations with and without hardening. In such cases, increasing the core strength to reflect the thinness effect does little to change the response (Fig. 8d).

5.3. Stress/displacement distributions

The stress distributions in the beams calculated for two of the configurations are shown in Fig. 9: one for a test in the core-shear domain (Fig. 9a) and the other for a test expected to exhibit indentation (Fig. 9b). In the former, the quite uniform stress in the core between the loading plattens, along with minimal reduction in the face sheet spacing, affirms the dominance of core shear. Note also that the stress in the core decreases slightly as the displacement increases, indicative of the development of hydrostatic stress in this region, which lowers the shear yield strength (Eq. (2)). In the other simulation (Fig. 9b), indentation of the core beneath the inner platten decreases the space between the face sheets as well as stretching them. Note that, because of the softness of the core, the upper face sheets exhibit bending stresses, with tension on the top and compression at the bottom.

The displacements of the underside of the beam, at its midpoint, relative to those for the load platten, indicate the level of indentation taking place (Fig. 10). Where indentation is expected, there is indeed a difference in these displacements. In configurations where core shear dominates, there is no such difference. However, one consistent disparity arises when a weak face sheet is used. In such cases, some indentation occurs even when the design is in the core-shear domain.
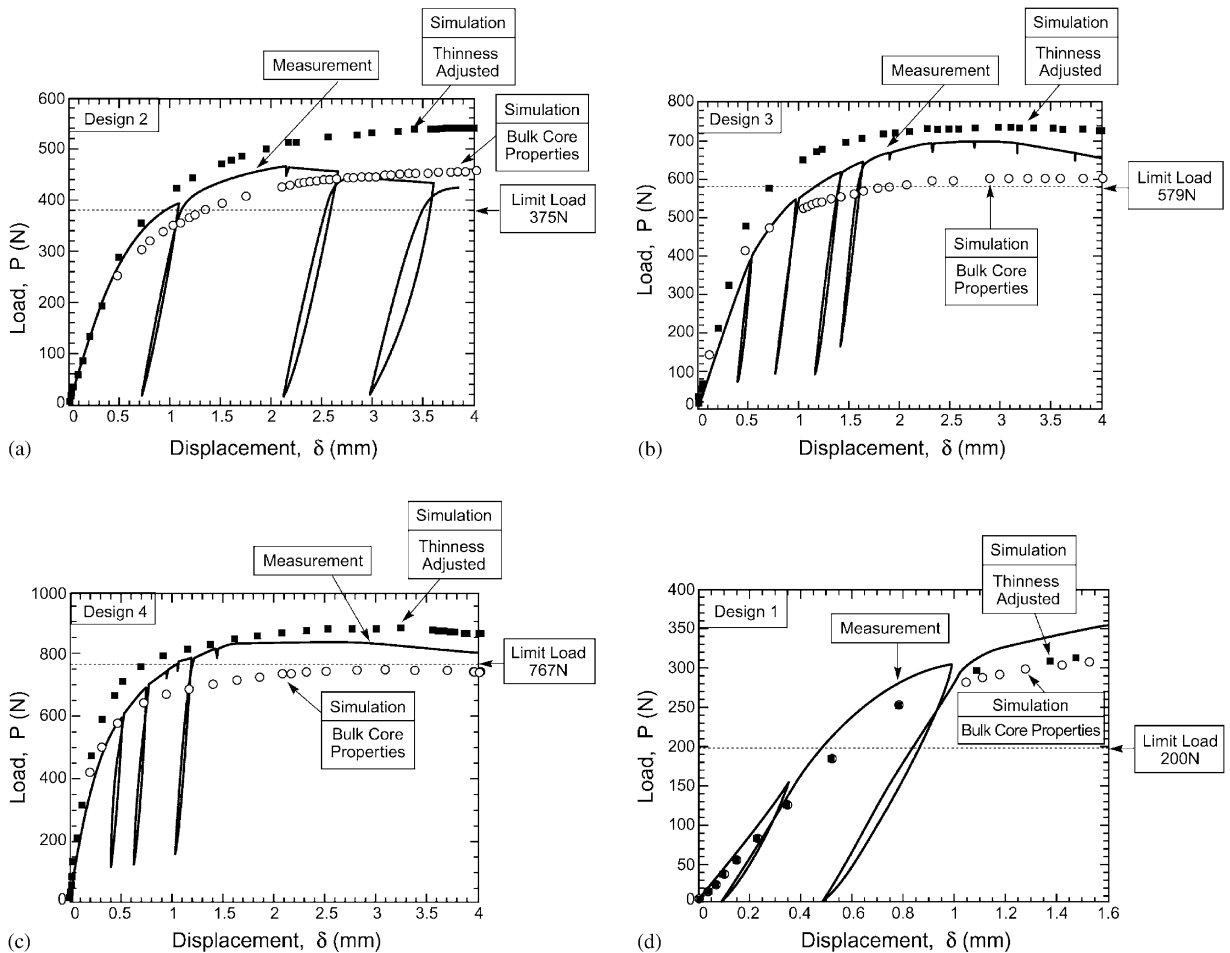
Fig. 8. Characteristic load–deflection curves calculated by finite elements for different modes of failure, overlaid with experimental results.

Some discrepancies arise for configurations at (or close) to the transition between core shear and indentation. Designs just within the core shear domain experience indentation of the center fixture — in some instances by a considerable amount — suggesting that the boundary between the two modes found from the analytical model is prone to some inaccuracy. Accordingly, the appropriate procedure would be to estimate the domains on the mechanism maps by using the analytical model and then use the numerical results for adjustments and refinements.

6. Comparison between analytical and numerical results

6.1. Limit loads

Limit loads calculated from the analytical expressions all underestimate those experimentally achieved, Table 4 in Appendix B. The largest discrepancy involves cases where face yielding is the
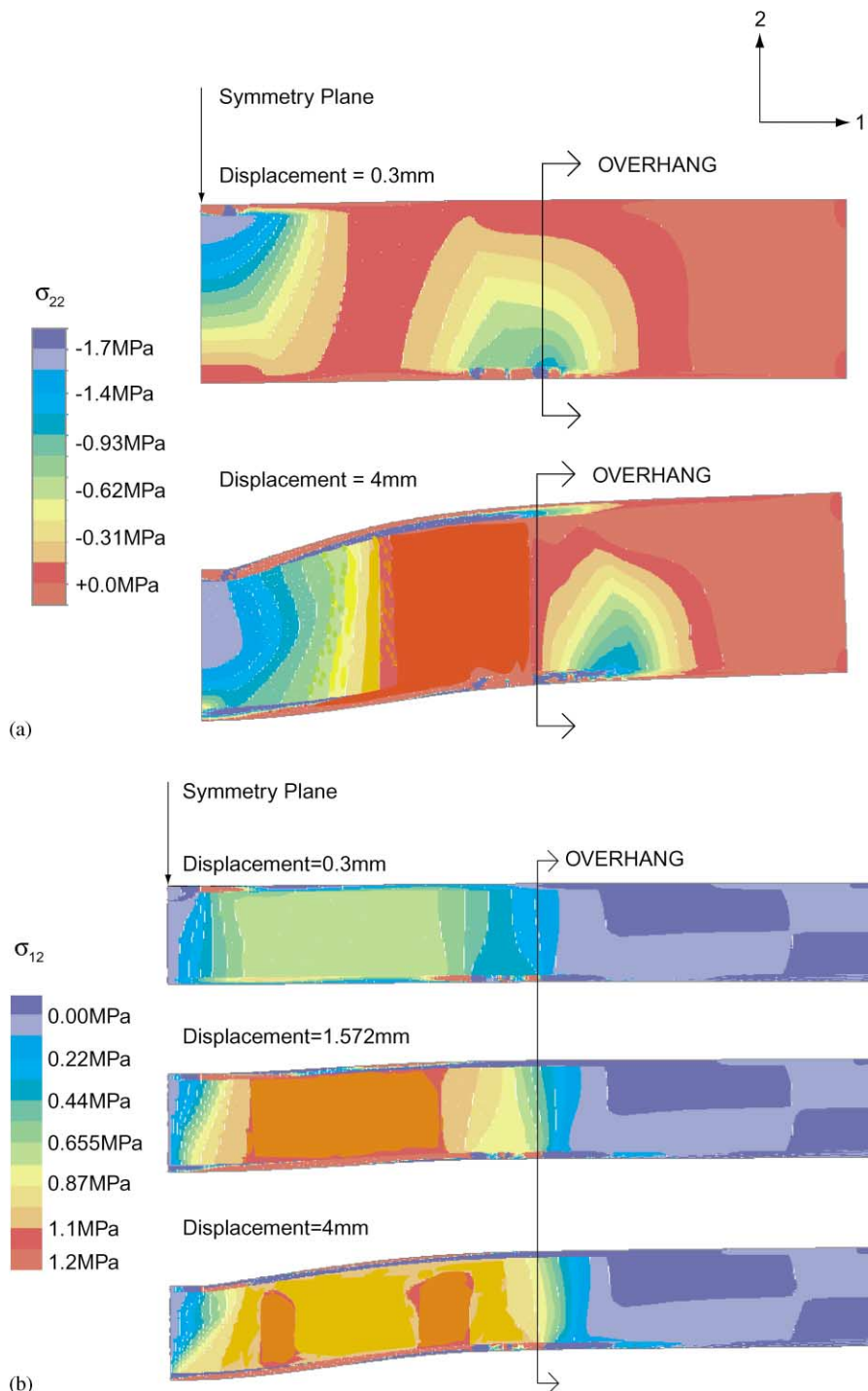
Fig. 9. Finite element results showing the stress distributions. (a) Specimen that fails by indentation. Notice the significant plastic deformation within the bottom face sheet in addition to indentation by the loading fixture. (b) Specimen that fails by core shear. Notice the shear deformation of the core within the overhang.
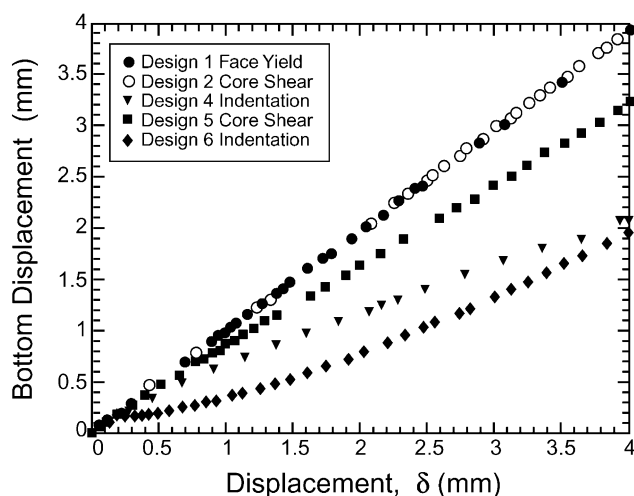
Fig. 10. Calculation of the level of indentation taking place in various specimens.

dominant failure mode. In Fig. 8d, the analytical limit load is only one-half that found experimentally, with marginal improvement when the effects of the core are included. The discrepancy has been attributed to the nature of the experiment where, in order to simulate face yielding, a large R/L ratio was chosen. In developing the analytical solutions (Eq. (A.6a)) it was assumed that the beam is long, in accordance with Timoshenko beam theory, wherein the load is represented by a concentrated force at the midpoint of the beam. The beams tested cannot be considered long and thus limit-load calculations of this type are incorrect. The numerical simulations are designed to match the experiments (with the load distributed over $2R$). These indicate more complex behavior wherein face sheet yielding is initiated before plastic deformation in the core takes place (Fig. 10).

For cases where core yielding and indentation are the dominant modes of failure, the limit-load calculations are closer to the maximum attained in the experiments (and even closer to the numerical simulations where the bulk core properties are used). In these cases, R/L is considerably smaller, affirming that this parameter is influential in the difference between the analytical and numerical results.

6.2. Deformation mechanisms

Examination of the numerical results yields interesting insights into the deformations mechanisms. Comparisons can be made between the analytical assumptions (plastic hinge formation, etc.) and the results found using finite element simulations. Analytically, for indentation, it is assumed that four plastic hinges form on the upper face sheet with the core under compression. It is clear from the stress plots that the upper face sheet displays plastic hinges — one at the edge if the flat punch fixture and another some distance away from this edge. While the expected core indentation does take place, note that the bottom face sheet also experiences plastic deformation (Fig. 9a).

As mentioned earlier, the core-shear analysis used to construct the failure map assumes that plastic hinges form at the mid-span and at the outer supports, with no shearing taking place in the

Table 3
Bending compliance comparison

Design #	Analytical Π Initial loading	Numerical Π Initial loading	Experimental Π Initial loading
1	439	300	260
2	239	133	133
3	207	167	200
4	181	147	139
	Unloading	Unloading	Unloading
1	300	181	179
2	107	79	84
3	73	58	52
4	48	44	38

overhang (Fig. 14b). Examination of the stress plots (Fig. 9b) displays the combined effect of plastic hinge formation at the outer supports and core shear deformation in the overhangs. The deformation suggests that core failure is a combination of the two modes described in the appendix (Eqs. (A.9) and (A.10)). Despite this complication, the analytical calculations using Eq. (A.10) provide a reasonable representation of the measured response.

6.3. Stiffness

Comparison between the bending stiffness predicted for both initial loading and unloading with those found from the measurements is facilitated by plotting the compliance index, Π (Eq. (A.2): given in Table 3), against the dimensionless span: $\beta \equiv [(t/L)(c/L)]^{-1}$. For the analytical model, such a plot should have a slope $\frac{1}{24}$ and intercept, $E_f/4G_c$, (Eq. (A.2)) as shown in Fig. 11. The comparison for unloading (Fig. 11, which exhibits the least variability) reveals consistency between the measurements and the numerical predictions. Conversely, while the analytical model predicts compliances consistent with measurements when β is small, it appreciably overestimates Π at larger β. The results at larger β coincide with configurations wherein R/L is relatively large. Again, therefore, the discrepancy appears to reside in the simplification inherent in the use of Timoshenko beam theory. This conclusion is in accordance with the results obtained by Andrews et al. [10].

7. Implications

The correspondences described above between the measured and simulated load/deflection curves (Fig. 8), as well as among the associated failure mechanisms (Figs. 9 and 10), are generally quite acceptable. The correspondence affirms the utility of the Deshpande and Fleck [4] constitutive law and its numerical implementation for the conduct of design calculations on sandwich configurations. In all cases, upon using the bulk properties for the core, the peak load capacities of
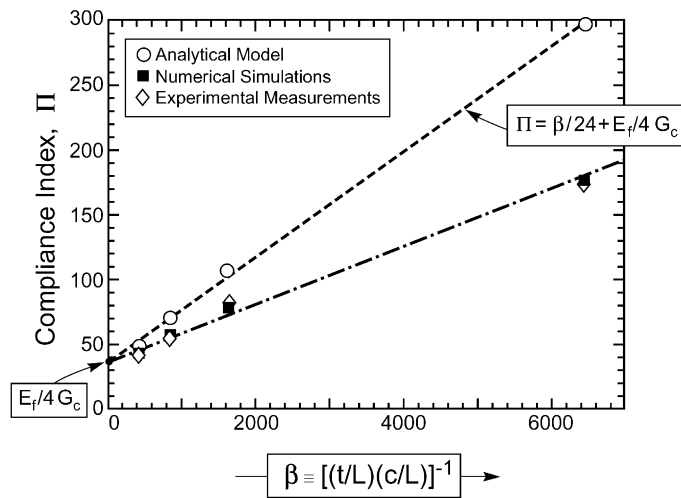
Fig. 11. Comparing analytical, numerical, and experimental values of the non-dimensional compliance index, Π, for unloading: calculations based upon unloading modulus of the core.

the beams are somewhat underestimated. It is suggested that these results be used as conservative estimates for design purposes. The elementary core thinness adjustment used in this study over-compensates for the interaction between the core and the face sheets. The discrepancies probably arise because the epoxy used to bind the core to the faces allows some rotation of the embedded cell walls. Care must be taken when using analytical solutions to predict failure and stiffnesses. As R/L becomes large (> 0.1) the reliability of analytical solutions becomes questionable.

Appendix A. Summary of failure load solutions

A.1. Bending stiffness

The compliance of a sandwich beam is [7,11]:

$$C \equiv \delta/P = \frac{2L^3}{B_1 E_f btc^2} + \frac{L}{B_2 G_c bc}. \tag{A.1}$$

The faces have thickness t, Young's modulus E_f, and the core has thickness c, and shear modulus G_c. The beam has span length L and width b, and in three point bending, $B_1 = 48$, $B_2 = 4$: whereupon the compliance has the non-dimensional form

$$\Pi \equiv CE_f b(c/L) = (1/4)\left[\frac{1}{6(t/L)(c/L)} + E_f/G_c\right]. \tag{A.2}$$

A.2. Initial yielding

A.2.1. Core shear

In analyzing initial *failure of the core*, both the shear and normal components of stress have been taken into account. It is not appropriate to assume that the normal stresses in the core are small compared with the shear stresses, because the strength of the Alporas is not insignificant relative to that for the face sheet materials. Using the yield condition (Eq. (2)), with the effective and mean stresses expressed as a function of the load, the critical load is [4,12]

$$\bar{P}_{CY} = \left[\frac{1 + (\alpha/3)^2}{\gamma^2(1 - v + v^2) + 3\beta^2 + \alpha^2\gamma^2[(1 + v)/3]^2} \right]^{1/2},$$

$$\gamma = \frac{E_c/E_f}{B_3(t/L)(c/L)}, \quad \beta = \frac{1}{B_4(c/L)}. \tag{A.3}$$

The parameter α is obtained from Fig. 4 and v is the elastic Poisson ratio of the core. For three-point bending, the coefficients are $B_3 = 4$ and $B_4 = 2$.

A.2.2. Indentation

Following Miller [13], the load necessary to initiate indentation was found by determining the effect of varying the key material and geometric parameters on the load–displacement response. An upper bound analysis was carried out to determine the load variable (Fig. 12). An energy argument was used to derive a simple normalizing scheme for the displacement [12]. The ensuing set of load–displacement curves revealed that the onset of indentation occurred at

$$\bar{P}_I = 1.4 \left(\frac{1}{\sqrt{2}} \sqrt{\frac{\sigma_Y}{\sigma_c}} \frac{t}{L} + \frac{R}{L} \right), \tag{A.4}$$

where σ_c is the yield strength of the core and σ_Y is the yield strength of the face sheet.

A.3. Limit loads

A.3.1. Face sheet yielding

The maximum in-plane stress in the face sheets in three-point bending is given by

$$\sigma = (1/4) \frac{(P/bL)}{(c/L)(t/L)}. \tag{A.5}$$

Consequently, in the absence of stress redistribution effects, the loads carried by the system when the face sheets experience yielding become

$$P_{fY} = 4\sigma_Y bL(c/L)(t/L) \tag{A.6a}$$

or

$$\bar{P}_{fY} = 4\left(\frac{\sigma_Y}{\sigma_c}\right)\left(\frac{c}{L}\right)\left(\frac{t}{L}\right). \tag{A.6b}$$
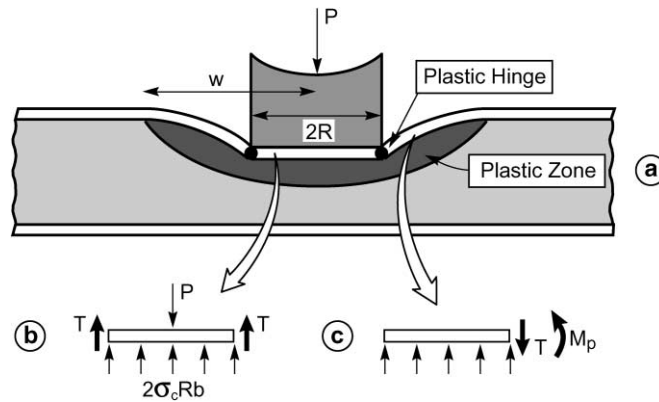
Fig. 12. Schematic of indentation failure showing the deformations used to determine the initial failure load as a function of geometric and material parameters.
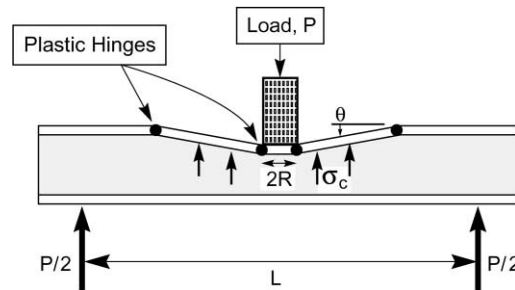

Fig. 13. Schematic of indentation failure showing the deformations used to determine the limit load.

This estimate neglects the effect of the core when calculating the plastic collapse moment. Also, the thickness of the face sheet is assumed small, $c + t \approx c$.

A.3.2. Indentation

An upper-bound calculation has been used to determine the collapse load for indentation. In this calculation, the upper face is witness to the formation of four plastic hinges (Fig. 13). The core yields in compression over an area, $2b(R + \lambda)$, where λ is a free variable determined by a minimization of the upper-bound solution,

$$P = \frac{4M_P}{\lambda} + b(2R + \lambda)\sigma_c, \tag{A.7}$$

where M_P is the plastic moment for the face sheet. Upon assuming that the indentation yield strength of the core at the center loading point is the same as that for uniaxial compression, then through a force balance, the indentation load becomes

$$\bar{P}_I = 2\sqrt{\frac{\sigma_Y}{\sigma_c}\frac{t}{L}} + 2\frac{R}{L} \tag{A.8}$$

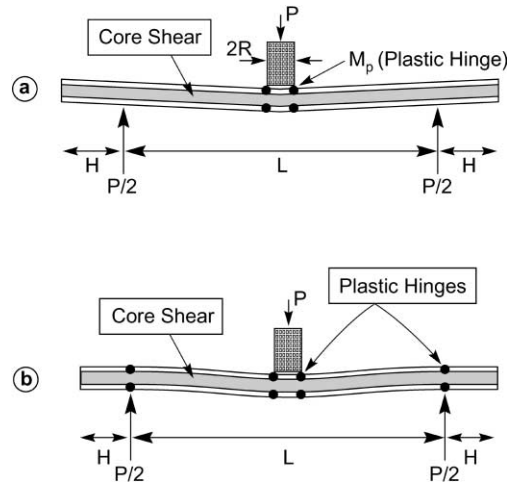which exceeds that for initial yield (A.4) by about a factor of 2.

Fig. 14. Schematics of two kinematically admissible displacement fields for failure by core shear.

A.3.3. Core shear

For core-shear failure, two kinematically admissible displacement fields are considered (Fig. 14). The first invokes the formation of plastic hinges at the edges of the flat punch and shearing deformation of the core over its entire length. A work balance then gives

$$\bar{P}_{CS1} = 2\left(\frac{t}{L}\right)^2 \frac{\sigma_Y}{\sigma_c} + 2\frac{c}{L}\left(1 + \frac{2B}{L}\right)\frac{\tau_c}{\sigma_c}, \tag{A.9}$$

where B is the length of the overhang and τ_c is the shear yield strength of the core: $\tau_c \approx (\frac{2}{3})\sigma_c$.

The alternative approach assumes plastic hinges at the mid-span as well as the outer supports, such that no shearing takes place within the overhang. Equating the external and internal work done, the upper-bound solution is

$$\bar{P}_{CS2} = 4\left(\frac{t}{L}\right)^2 \frac{\sigma_Y}{\sigma_c} + 2\frac{c}{L}\frac{\tau_c}{\sigma_c}. \tag{A.10}$$

In practice, one must look at the length of the overhang to determine which expression is appropriate. As both are upper-bound calculations, which ever gives the lower load, for a given beam design, must be used. (Eq. (A.10)) is used because the overhang, B, chosen for the experimental measurements is relatively large.

Appendix B. Addendum

B.1. Recalculation of limit load for face yielding of simply supported sandwich beam with distributed load

The original analysis used to calculate the limit load for face yielding is simplified on two counts. The first neglects the effect of the core. The second assumes that the beam is loaded under

Table 4
Initial yield and limit load comparison

Design No.	Analytical Initial yield (N)	Numerical (bulk properties) Initial yield (N)	Experimental Initial yield (N)
1 (FY)	—	190	230
2 (CS)	218	200	225
3 (CS)	427	320	400
4 (I)	405	320	360
	Limit load (N)	Limit load (N)	Limit load (N)
1 (FY)	200	320	355
2 (CS)	375	460	460
3 (CS)	579	610	700
4 (I)	767	750	840

Table 5

Design 1: Limit-load comparison Experiment (N)	Simple (N)	Extended (N)	Distributed (N)
355	200	231	272

a concentrated force. For small R/L this assumption suffices, but as R/L increases the calculated limit load under predicts that found experimentally. This is clearly the case for Design 1. Revoking the first assumption narrows the difference with experiment but not satisfactorily. Relaxing the point force assumption and requiring that the force, P, be applied over a span $2R$ resolves the disparity. In this case, the maximum moment along the length of the beam is

$$M^{\mathrm{max}} = \frac{P}{4}(L - R). \qquad (B.1)$$

Equating this moment to the plastic moment of the section ($M^P = \sigma_Y tb(c + t) + (1/4)bc^2\sigma_c$) gives the limit load for face yielding (Table 4):

$$P_{fY} = \frac{4\sigma_Y tb(c + t)}{L - R} + \frac{\sigma_c bc^2}{L - R}. \qquad (B.2)$$

Table 5 demonstrates the effect of increasing the accuracy of the analytical analysis. The detailed limit-load calculation improves the comparison with experiment, although it still somewhat underestimates the maximum load.

References

[1] Ashby MF, Evans AG, Fleck NA, Gibson LG, Hutchinson JW, Wadley HGN. Metal foams: a design guide. London: Butterworth Heinemann, 2000.

[2] Evans AG, Ashby MF, Hutchinson JW. Progress in Material Science 1999;43:171–221.

[3] Budiansky B. International Journal of Solids and Structures 1999;36:3677–708.

[4] Deshpande VS, Fleck NA. Isotropic constitutive models for metallic foams. Journal of the Mechanics and Physics of Solids 2000;48(6):1253–83.

[5] Akiyama S et al., US Patent 4,713,277, December 15, 1987.

[6] Sugimura Y, Meyer J, He MY, Bart-Smith H, Grenestedt J, Evans AG. Acta Materialia 1997;45(12):5245–59.

[7] Gibson LG, Ashby MF. Cellular solids. Cambridge: Cambridge University Press, 1997.

[8] Bastawros A-F, Bart-Smith H, Evans AG. Journal of the Mechanics and Physics of Solids 1999;48(2):301–22.

[9] Chen C, Manual for a UMAT user subroutine. Cambridge Centre for Micromechanics, 1998.

[10] Andrews EW, Gioux G, Onck PR, Gibson LJ. Size effects in ductile cellular solids, Part II: experimental results. International Journal of Mechanical Sciences 2001;43(3):701–13.

[11] Allen HG. Analysis and design of structural sandwich panels. Oxford: Pergamon Press, 1969.

[12] McCormick TM, Miller R, Kesler O, Gibson LJ. Failure of sandwich beams with metallic foam cores, 2000, to be published.

[13] Miller RE. A continuum plasticity model for the constitutive and indentation behavior of foamed metals. International Journal of Mechanical Sciences 2000;42(4):729–54.

[14] Onck PR, Andrews EA, Gibson L. Size effects in ductile cellular solids, Part I: modelling. International Journal of Mechanical Sciences 2001;43(3):681–99.

Further reading

Bart-Smith H, Bastawros A-F, Mumm DR, Evans AG, Sypeck DJ, Wadley HNG. Acta Materialia 1998;46(10):3583–92.

Chen C, Harte A-M, Fleck NA. The plastic collapse of sandwich beams with a metallic foam core. International Journal of Mechanical Sciences, 2000, submitted for publication.

Gioux G, McCormack TM, Gibson LJ. Failure of aluminum foams under multiaxial loads. International Journal of Mechanical Sciences 2000;42(6):1097–117

McCullough KYG, Fleck NA, Ashby MF. Acta Materialia 1999;47(8):2323–30.